JOURNAL OF GEOPHYSICAL RESEARCH, VOL. 114, B02213, doi:10.1029/2008JB005632, 2009

Micron-scale roughness of volcanic surfaces from thermal infrared spectroscopy and scanning electron microscopy

Adam J. Carter,[1] Michael S. Ramsey,[1] Adam J. Durant,[2,3] Ian P. Skilling,[1] and Amy Wolfe[1]

Received 14 February 2008; revised 9 September 2008; accepted 3 December 2008; published 27 February 2009.

[1] Textural characteristics of recently emplaced volcanic materials provide information on the degassing history, volatile content, and future explosive activity of volcanoes. Thermal infrared (TIR) remote sensing has been used to derive the micron-scale roughness (i.e., surface vesicularity) of lavas using a two-component (glass plus blackbody) spectral deconvolution model. We apply and test this approach on TIR data of pyroclastic flow (PF) deposits for the first time. Samples from two PF deposits (January 2005: block-rich and March 2000: ash-rich) were collected at Bezymianny Volcano (Russia) and analyzed using (1) TIR emission spectroscopy, (2) scanning electron microscope (SEM)-derived roughness (profiling), (3) SEM-derived surface vesicularity (imaging), and (4) thin section observations. Results from SEM roughness (0.9–2.8 μm) and SEM vesicularity (18–26%) showed a positive correlation. These were compared to the deconvolution results from the laboratory and spaceborne spectra, as well as to field-derived percentages of the block and ash. The spaceborne results were within 5% of the laboratory results and showed a positive correlation. However, a negative correlation between the SEM and spectral results was observed and was likely due to a combination of factors; an incorrect glass end-member, particle size effects, and subsequent weathering/reworking of the PF deposits. Despite these differences, this work shows that microscopic textural heterogeneities on PF deposits can be detected with TIR remote sensing using a technique similar to that used for lavas, but the results must be carefully interpreted. If applied correctly, it could be an important tool to map recent PF deposits and infer the causative eruption style/mechanism.

Citation: Carter, A. J., M. S. Ramsey, A. J. Durant, I. P. Skilling, and A. Wolfe (2009), Micron-scale roughness of volcanic surfaces from thermal infrared spectroscopy and scanning electron microscopy, *J. Geophys. Res.*, *114*, B02213, doi:10.1029/2008JB005632.

1. Introduction

1.1. Vesicularity and Surface Change Detection

[2] Changes in the vesicularity of active lava domes and flows can provide useful information on the volatile content and degassing history, for example, which can be used to infer the risk of impending explosive activity [*Anderson and Fink*, 1990]. Calculating the vesicularity of in-situ samples is commonly difficult and dangerous on active volcanoes. However, a collected sample can be analyzed using several techniques: optical microscopy [e.g., *Sarda and Graham*, 1990], the application of Archimedes' principle [*Houghton and Wilson*, 1989], and the analysis of digital images collected by scanning electron microscope (SEM) [e.g., *Heiken and Wohletz*, 1985; *Klug and Cashman*, 1994]. In addition, modern three-dimensional imaging techniques such as Synchrotron X-ray microtomography have been used to generate accurate volume estimates of vesicular rocks [e.g., *Song et al.*, 2001]. This technique has also been applied in other disciplines to quantify the surface characteristics of various substances at the micron scale [e.g., *Minnich et al.*, 2001; *Podsiadlo and Stachowiak*, 1997]. However, few studies have concentrated on the use of stereo images to analyze both two- and three-dimensional samples of volcanic materials.

[3] The surfaces of eruptive products can undergo rapid textural changes during active volcanism due to degassing, explosions, erosion/weathering, and the emplacement of new deposits. For example, pyroclastic density currents, lahars, as well as lava dome building and destruction phases have been observed at Soufrière Hills Volcano Montserrat [*Watts et al.*, 2002], Mt. Unzen, Japan [*Nakada et al.*, 1995] and Mt. Saint Helens, USA [*Anderson and Fink*, 1990; *Vaughan et al.*, 2005]. At all of these volcanoes the deposits underwent rapid surface change during activity. Macroscale (i.e., meter scale and above) changes can be easily observed and analyzed using high-resolution aerial and satellite images in order to monitor the emplacement of new deposits, secondary

[1]Department of Geology and Planetary Science, University of Pittsburgh, Pittsburgh, Pennsylvania, USA.
[2]Geological Sciences, Michigan Technological University, Houghton, Michigan, USA.
[3]Department of Earth Sciences, University of Bristol, Bristol, UK.

0148-0227/09/2008JB005632$09.00

reworking, and larger scale topographic changes [e.g., *Francis et al.*, 1996]. However, microscopic-scale detection and change require analysis at a resolution several orders of magnitude greater than what is available from satellites and aerial images. Of particular interest is the micrometer (micron)-scale (1–100 μm) of the surface products because it can alter and affect thermal infrared (TIR) energy emitted at the same scale. For example, particle size effects and surface textures such as vesicularity and micron-scale roughness can all be derived from morphological changes in the emitted TIR spectra [*Moersch and Christensen*, 1995; *Ramsey and Fink*, 1999; *Kirkland et al.*, 2002].

[4] For the work presented here, we compare the merits and limitations of several different data sets to estimate the surface vesicularity and micron-scale roughness (here on serving as a proxy for surface vesicularity) in samples of pyroclastic flow (PF) deposits from Bezymianny Volcano, Russia. The primary goal was to assess how accurately satellite-derived thermal emission spectra could be modeled in order to extract this roughness and map the percentages of blocks and ash on the surface, all of which relay important clues about the eruption style that produced the deposit. Here, we compare the laboratory- and satellite-based TIR spectral model results to (1) field-based mapping of the percentages of blocks and ash on two different PF deposits, (2) the surface vesicularity derived from SEM images of samples collected in the field, and (3) the SEM surface roughness derived from the profiling measurements of these same samples. This work tests the TIR remote sensing technique described by *Ramsey and Fink* [1999] and *Ramsey and Dehn* [2004], applying it for the first time to PF deposits. The information extracted from such an approach is critical for any active volcano where field mapping is too dangerous or for any remote volcano where the actual eruption responsible for the PF deposit was not observed.

1.2. Eruptive Products of Bezymianny Volcano

[5] Bezymianny (55.98°N, 160.58°E, ~2900 m altitude) is an active composite volcano on the Kamchatka Peninsula, Russia that averages one to two eruptions per year [*Bogoyavlenskaya et al.*, 1991; *Belousov et al.*, 2002; *Ramsey and Dehn*, 2004]. Its name ("no name" in Russian) was given by scientists during visits prior to 1955 because of its assumed insignificance and inactivity compared to its much larger neighbor, Klyuchevskoy Volcano. Bezymianny became well known after its March 1956 Plinian eruption, which created a directed lateral blast, sector collapse, and very large PF deposit [*Gorshkov*, 1959]. The eruptive products are typically basaltic-andesites and andesites with a SiO_2 range of 52.5% to 65.5% [*Bogoyavlenskaya et al.*, 1991]. Since 1956, a new lava dome has grown to ~2900 m [*Bogoyavlenskaya and Kirsanov*, 1981], and it currently exceeds the height of the 1956 collapse scar.

[6] On 14 March 2000, the Kamchatka Volcanic Eruption Response Team (KVERT) reported continuous volcanic tremor and indicated an eruption was in progress [*KVERT*, 2007]. An ash cloud traveled ~8 km above sea level (ASL) and a sizeable ash-rich PF traveled east into both branching valleys on the volcano [*Ramsey and Dehn*, 2004]. Nearly five years later (11 January 2005), an explosive eruption was recorded by seismic data [*KVERT*, 2005]. It produced an ash plume 8–10 km ASL and a block-rich PF deposit, which traveled 3 km from the vent. This was a typical run out distance for the numerous smaller eruptions observed over the past seven years [*Carter et al.*, 2007, 2008].

2. Background

2.1. Bezymianny Sample Descriptions

[7] We surveyed these recent (i.e., emplaced within the last 8 years) PF deposits in August 2005 along the eastern flank and into the southeast branching valley (Figures 1a–1d). The PF deposits were mapped using Global Positioning System (GPS) data and surveyed to assess the percentages of block and ash. These 90 square meter "pixel surveys" corresponded to the corners of one Advanced Spaceborne Thermal Emission and Reflection Radiometer (ASTER) TIR pixel. Each was chosen after careful examination of the ASTER data prior to the field campaign. The goal was to characterize the March 2000 and January 2005 PF deposits and assess the dominant surface cover. Therefore although many pixels were surveyed in the field, only two were selected for this study and presented here. The first was on the 11 January 2005 deposit (area 1) and the second was on the March 2000 deposit (area 2). Both sites were nonvegetated and consisted of unconsolidated and slightly reworked deposits.

[8] Numerous survey transects were performed and the areal percentages of blocks (i.e., >64 mm) and ash (i.e., <2 mm) were noted. During the surveys, both block and ash samples were collected randomly, described, and located using GPS. The surface of area 1 was covered with approximately 30% blocks and 70% ash from the January 2005 eruption. Samples MTU-2006-004 and -005 (here on referred to as -004 and -005) were collected from a random representative pyroclastic block within this region (Figure 1e). The block measured 1.5 m high and was rounded by abrasion during transport within the PF. Sample -004 was taken from the exterior surface and was considered the dominant block type within this area. Sample -005 was taken from the interior, which was partially exposed. This sample was not a major end-member for the surface cover, but was chosen in order to examine any textural heterogeneity within the blocks and to assess the degree of vesiculation during eruption. This block, and others in the deposit, were mechanically fragmented during emplacement, occasionally exposing a gray/black interior (sample -005) relative to the lighter grey outer surface (sample -004). The March 2000 deposit (area 2) was far more ash-rich (10% blocks and 90% ash) and was further weathered compared to the more recent January 2005 deposit. Ash sample MTU-2006-001 (here on referred to as -001) was collected at this site.

2.2. TIR Emission Spectroscopy Background

[9] TIR remote sensing and laboratory spectroscopy provide a nondestructive, quantitative means to collect information on the temperature, chemistry, and texture of a sample. The TIR radiance of the sample's surface is a function of the wavelength-dependent emissivity (ε) and its brightness temperature. These terms must be separated in order to analyze the emissivity spectrum [e.g., *Realmuto*, 1990]. In a five band image (e.g., ASTER TIR) for example, there will be six unknowns: five emissivity values and one brightness temperature. Thus an underdetermined set of

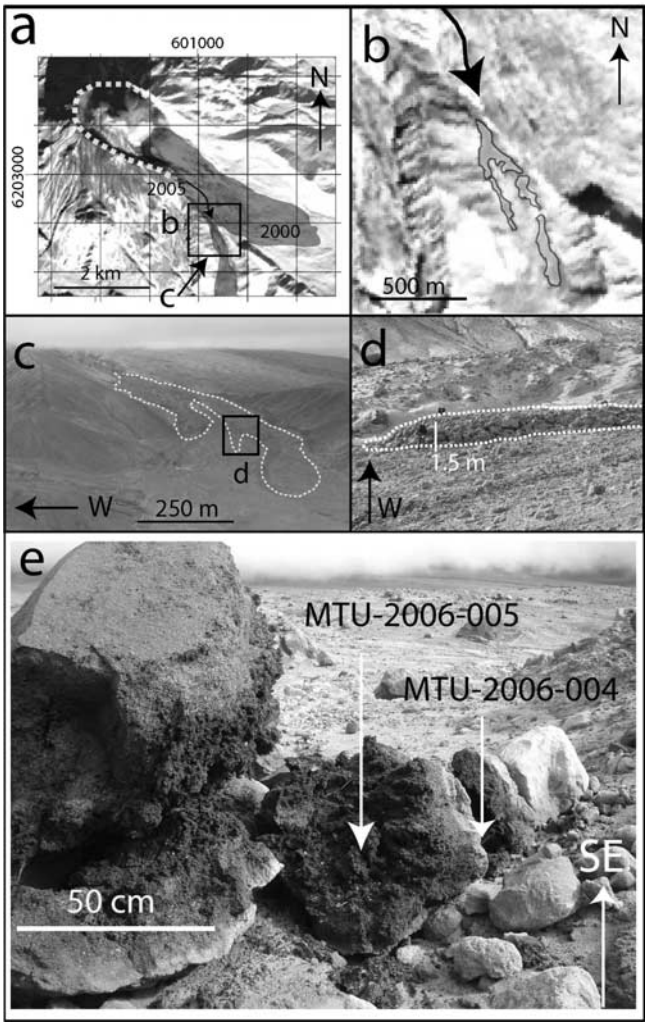

Figure 1. (a) ASTER image acquired on 23 January 2005 (UTM grid shown) showing the Bezymianny lava dome surrounded by the c-shaped 1956 crater (white dashed lines) and pyroclastic flow sheet to the southeast. The March 2000 PF is shown as a shaded area and the direction of the January 2005 PF is shown entering the southeast branching valley. (b) Outline of the January 2005 PF within the valley. (c) Aerial image taken in August 2005 showing the outline of the January 2005 PF. (d) Field image of the block-rich lobes within the January 2005 PF. (e) Blocks from the January 2005 PF deposit in the southeast branching valley. Two distinct textures were observed: a grey surface rind (MTU-2006-004) and a black interior (MTU-2006-005).

equations is produced, making one assumption necessary (e.g., the emissivity in one of the wavelength bands) in order to solve the set of Planck equations [e.g., *King et al.*, 2004]. The derived emissivity spectrum can then be used to determine: (1) the material composition [e.g., *Lyon*, 1965; *Christensen et al.*, 2000] or (2) the surface textures such as roughness and degree of glassiness [*Crisp et al.*, 1990; *Ramsey and Fink*, 1999; *Byrnes et al.*, 2004; *King et al.*, 2004; *Carter et al.*, 2006].

[10] The TIR spectral features of most mixtures are assumed to be linearly proportional to the areal abundance of the mixed end-members [e.g., *Adams et al.*, 1986; *Thomson and Salisbury*, 1993]. Therefore a linear, least-squares algorithm, in combination with a library of likely end-member spectra, can generally be used to identify the spectral components of the mixture and derive their abundances, and hence deconvolve or unmix the spectra. This approach has been widely used for compositional analysis both in the laboratory and from space [*Ramsey and Christensen*, 1998; *Feely and Christensen*, 1999; *Christensen et al.*, 2000; *Hamilton and Christensen*, 2000]. However, a potential complication to the approach of using laboratory-derived end-members applied to satellite-based remote sensing is the common phenomenon of reduction in spectral contrast of the latter as compared to the same linear mixture of end-members from the laboratory. This has been studied by several authors and is caused by a combination of factors, including incomplete atmospheric correction for either the direct (up-welling) energy or the reflected (down-welling) energy; the scattering of emitted energy from smaller (<50 μm) particles on the surface; the "cavity effect" of surface micron-scale roughness; and/or reflected side-welling energy from other surface features/particles. To first order all these processes can result in an additive effect of some percentage of either featureless blackbody spectral component or reflected energy with a similar (but opposite sign) spectral component. The latter has the same effect as adding blackbody to the TIR emissivity spectrum, and therefore both effects can be simply modeled and removed in the deconvolution approach [*Hamilton and Christensen*, 2000; *Kirkland et al.*, 2002; *Moersch et al.*, 2002].

[11] Previous studies have also applied this approach using only obsidian glass and a blackbody as end-members. Vesicles on glassy lava flows act as near-blackbody emitters, because emitted photons within these cavities commonly undergo multiple interactions with the vesicle walls before reaching the detector [*Ondrusek et al.*, 1993; *Ramsey and Fink*, 1999; *Ramsey and Dehn*, 2004]. The combined emitted and reflected components of these multiple interactions serve to reduce the spectral contrast in a linear manner proportional to the micron-scale roughness [*Ramsey and Fink*, 1999]. Thus the spectral contrast was used to define a quantitative estimate of the percentage of surface vesicularity (i.e., a smaller contrast suggesting a greater vesicularity and vice versa). *Ramsey and Fink* [1999] constructed an algorithm capable of creating a map-based estimate of surface vesicularity on glassy rhyolite lava flows, which was validated with field maps and SEM images of cross-sectional cuts through the surface of the various pumice textures. Samples studied included an obsidian, finely vesicular pumice and coarsely vesicular pumice. The absorption depth (or spectral contrast) of the primary Si-O Restrahlen band was shown to decrease with increasing vesicularity and was detectable with airborne TIR remote sensing.

[12] *Ramsey and Dehn* [2004] expanded this approach to space-based TIR data collected over Bezymianny's active lava dome. Some complications arose on the dome due primarily to small-scale (subpixel) thermal heterogeneities as well as possibly from surface mineral deposits and fumarolic degassing, all of which have effects on the integrated TIR emission spectrum from any given pixel. However, they showed that the technique was still a valid approach for

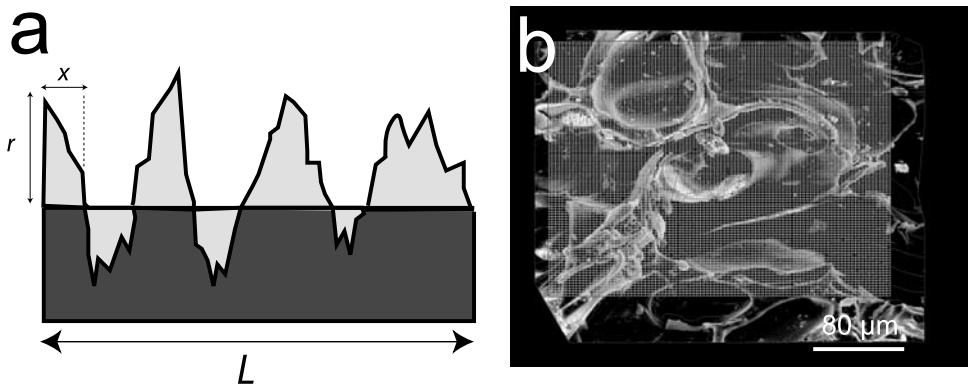

Figure 2. Surface roughness of PF samples derived from SEM stereology. (a) The average surface roughness (R_a) is the integral of the absolute value of the roughness profile of length, where L is the total length of the profile analyzed, and r is the height (z axis) difference relative to the mean height of the profile, measured along incremental distance x. (b) Example of image MTU-2006-004, with 200 horizontal and 200 vertical profile lines overlain (fine lines) to calculate R_a for each sample.

mapping detectable changes in surface roughness of the lava dome over time. In this work, we further expand this binary modeling approach to test its applicability to pyroclastic flows (PF).

2.3. ASTER Data Background

[13] ASTER acquires image-based data of reflected and emitted energy in the visible/near infrared (VNIR) region in three wavelength channels (0.56–0.81 μm) at 15 m/pixel spatial resolution, in the short-wave infrared (SWIR) region in six wavelength channels (1.65–2.40 μm) at 30 m/pixel spatial resolution, and in the TIR region in five wavelength channels (8.29–11.32 μm) at 90 m/pixel spatial resolution [*Yamaguchi et al.*, 1998]. The raw image data are corrected for geometry and band to band registration and later processed into on-demand, level 2 (L2) products such at-ground TIR radiance, brightness temperature, and surface emissivity [*Abrams*, 2000]. For this study, spectra were extracted from an ASTER TIR L2 emissivity product which was derived from an image acquired on 20 August 2005 at night (local time). The emissivity spectra from the pixels that corresponded to the location of the field samples and surveys were used for this analysis.

2.4. SEM-Derived Surface Roughness Background

[14] Roughness (or rugosity) is defined as a measurement of the small-scale variations in the height of a physical surface, or its lack of order [*Thomas*, 1999]. Each measured roughness profile is described by a waveform that has a range of frequency components; high-frequency or short-wavelength components are assumed to describe the *roughness* of the sample, whereas low-frequency or long-wavelength components are related to more gradual changes and describe waviness or form of the profile [*Thomas*, 1999]. The roughness is superimposed on the waviness of a given surface, and is responsible for changes in the TIR emissivity spectra. There are several methods for calculating the roughness. For engineering applications, a rapid, averaging method is commonly used to classify entire surfaces. The surface average roughness (R_a) is the integral of the absolute value of the roughness profile (the roughness value along a given line) relative to a mean line (Figure 2a) over an evaluation length [*ISO*, 1997]. The mean reference line is created after filtering the roughness and waviness components from the profile under investigation. The filter uses a least-squares fit, followed by separation of the short-wave component from the long-wave component. R_a is defined as

$$R_a = \frac{1}{L} \cdot \int_0^L |r(x)| d(x) \tag{1}$$

where L is the total length of the profile analyzed, and r is the height (z axis) difference relative to the mean height of the profile, measured along incremental distance x. Here, R_a was calculated from digital elevation models (DEMs) generated using SEM stereology.

3. Methods

3.1. Laboratory TIR Spectroscopy Methods

[15] Bezymianny samples were prepared for Fourier-Transform Infrared (FTIR) thermal emission spectroscopy [*Christensen et al.*, 2000; *King et al.*, 2004], following the approach used in *Ruff et al.* [1997]. Emission spectra of the samples were collected at the Thermal Emission Spectroscopy (TES) Laboratory at Arizona State University and Image Visualization and Infrared Spectroscopy (IVIS) Laboratory at the University of Pittsburgh. At both laboratories a Thermo-Nicolet Nexus 670 FTIR spectrometer with a temperature stabilized Deuterated Triglycine Sulfate (DTGS) detector was used to collect the TIR spectra. The spot size for each spectrometer was approximately 2 cm. However, the IVIS Laboratory used a potassium bromide (XT-KBr) beamsplitter at the time with a spectral range of 5–25 μm, whereas the TES Laboratory currently uses a Caesium Iodide (CsI) beamsplitter extending the range to 50 μm. The spectra of temperature-stabilized precision blackbodies were first acquired and used to calibrate the instrument response function [*Ruff et al.*, 1997]. The blackbodies and samples were placed in an environmental chamber, which was purged using air scrubbed of water vapor and carbon dioxide in order to minimize the spectral features from these TIR-active gases.

Table 1. Description of SEM Images of Samples Collected From the 14 March 2000 and January 2005 Pyroclastic Flow Deposits at Bezymianny

Sample	Eruption Date	Location (UTM, WGS-84)	Block/ Particulate	Average Vesicle Diameter (μm)	Brief Description
MTU-2006-001-P1	Mar 00	6199981.77 m N, 602378.80 m E	Particulate	<80	Single image of a lapillus 5 mm wide from within sample MTU-2006-001
MTU-2006-001-P4	Mar 00	6199981.77 m N, 602378.80 m E	Particulate	~30	Single image of an ash particle 300 μm long, 150 μm wide from within sample MTU-2006-001
MTU-2006-004	Jan 05	6200261.35 m N, 601986.869 m E	Block	<100	Taken from the outer surface of a rounded pyroclastic block within the January 2005 PF deposit; grey, visibly rough
MTU-2006-005	Jan 05	6200261.35 m N, 601986.869 m E	Block	<80	Taken from the interior of a rounded pyroclastic block that had fragmented during emplacement within the January 2005 PF deposit; black and less visibly rough than sample -004

[16] Prior to analysis, each sample was heated to 80°C in order to provide adequate thermal energy above the background energy/temperature of the laboratory. The warm samples were placed in the chamber and data collected for 256 scans (~9 minutes), which were averaged for higher signal to noise. For the coherent, lithic blocks (-004 and -005), small samples measuring approximately 40 mm wide by 20 mm thick were carefully chipped from a larger block. For the ash-lapilli sample (-001), approximately 2 g of ash filled one sample cup.

3.2. SEM Imaging and Stereogrammetry Methods

[17] SEM imaging was performed on the Bezymianny PF deposit samples. The same samples had first been measured using TIR emission spectroscopy prior to their preparation for the SEM analysis. A small portion of each sample was prepared with lateral dimensions of $\leq$10 mm diameter and a height of 7–8 mm. All samples were fixed to aluminum stubs using a wax adhesive (following the TIR analysis), coated using a gold sputter coater to a thickness of 15 nm. Image quality was enhanced through the application of silver paint between the sample and stub in order to improve the electrical ground. Homogenous ash particle dispersions for SEM analysis were prepared following a simple approach (O. P. Mills, personal communication, 2006). A small amount of ash was placed adjacent to an aluminum sample stub in a sealed plastic container; each stub had an electrically conductive adhesive coating on its upper surface. Several short bursts of pressurized gas were aimed at the ash sample through an opening in the top of the container, which dispersed ash particles evenly over the entire sample stub.

[18] Digital images were acquired on a JEOL JSM-6400 SEM at Michigan Technological University and processed using Alicona Imaging MeX software. The image magnification of 400 was optimized according to time and hardware constraints, and provided a resolution of 0.183 μm, which was adequate for analyzing the 1–100-μm scale surfaces. Three-dimensional characteristics were measured using a stereo pair of secondary electron images [e.g., *Podsiadlo and Stachowiak*, 1997]. *Goldstein et al.* [1981] provides a detailed explanation of the SEM image retrieval method. SEM images of the sample were captured at a separation angle of 6° (3° from either side of vertical) with the magnification and working distance held constant. The smallest aperture setting on the instrument (50 μm) was used to create a low convergence angle and the greatest depth of field. Imaging was conducted rapidly to limit sample coating degradation by the electron beam. A DEM was generated from these images and the morphology and surface area were analyzed to quantitatively measure the surface characteristics of each sample.

[19] After transport back to the University of Pittsburgh, all of the samples were prepared for more detailed analyses including the SEM imaging. Four SEM images were collected (Table 1). Samples -004 and -005 from the 11 January 2005 PF deposit (area 1) and two ash particles (-001-P1 and -001-P4) from the 14 March 2000 deposit (area 2) were imaged. We analyzed 200 horizontal and 200 vertical roughness profiles to investigate the variation in surface morphology (Figure 2b) and generated a single numerical R_a value for each sample (Table 2). The National Institutes of Health freeware/software application ImageJ was used to process SEM images [*Rasband*, 1997]. We created binary images that highlighted the vesicles/voids in black (DN = 0) and the glassy portion of the sample in white (DN = 255). A threshold level was manually set for each image to highlight the vesicular regions only. To ascertain the uncertainty associated with this approach, three images were selected and the threshold was varied to give a range of reasonable vesicularity estimates for each image. The error margin for this technique was calculated (±6%), taken from the range between maximum and minimum vesicularity estimates.

4. Results

4.1. Thin Section Analyses

[20] The mineralogy and surface texture were investigated using standard petrographic thin sections for samples -004, and -005. For sample -001, ash was impregnated with a resin before being prepared for thin section analysis. The primary aim was to assess the submillimeter-scale mineralogy and analyze the surface texture and vesicularity.

[21] Sample -001 was hypocrystalline and glomeroporphyritic, with crystals of plagioclase, hornblende (Hb), and clinopyroxene (CPX), including iron-rich alteration products, set in a glassy matrix that was prevalent throughout the sample. Crystals were inequigranular, present as phenocrysts and within crystal aggregates that displayed reaction textures, such as coronae and alteration products. Many

Table 2. Image-Derived Surface Vesicularity and R_a Values

Sample	SEM image Resolution (μm)	Magnification	Image-Derived Vesicularity (%)	R_a (μm)
MTU-2006-001-P1	0.1833	400	20	1.3
MTU-2006-001-P4	0.1833	400	18	0.9
MTU-2006-004	0.1833	400	26	2.8
MTU-2006-005	0.1833	400	22	1.6

Hb crystals could also be seen embedded within plagioclase laths and crystals. CPX crystals were mostly inequigranular, anhedral and degraded, some showing skeletal textures. Spherical vesicles were visible, commonly occupying the space between crystals.

[22] Sample -004 was hypocrystalline and porphyritic in thin section. The sample was highly vesicular and composed of discrete phenocrysts of plagioclase, Hb, and CPX was set in a glassy matrix. Qualitatively, sample -004 displayed a far higher vesicularity than sample -001 visible at this resolution. Sample -005 was similar in texture, mineralogy, and vesicularity to sample -004 as they were from the exterior and interior of the same pyroclastic block, respectively. Furthermore, at the magnification available, micrometer-scale vesicles were too small to be investigated, calling for the use of SEM images at a much higher magnification.

4.2. TIR Spectroscopy Results

[23] We used the two end-member approach of *Ramsey and Fink* [1999] to deconvolve the TIR emission spectra of each sample. The two end-members were a high-SiO_2 obsidian and an artificial blackbody (Figure 3). Thermal emission spectroscopy data were collected for the coherent block samples -004 (Figure 4), -005 (Figure 3), and particulate sample -001 (Figure 5). All the laboratory spectra of the samples had a similar morphology to the obsidian spectrum and fell within the range of the two end-member spectra, which indicated that they were likely a linear construct of the two end-members. Within sample -004 (Figure 4), residual errors between 9–11 μm and 15–22 μm may have been partially caused by slight differences in the glass compositions between the sample and end-member used [*Byrnes et al.*, 2007]. However, as shown by *Minitti et al.* [2007], the difference between emissivity minima for andesite and dacite were small, suggesting that a compositional difference in the modeled and real end-member was not a major contributor to errors.

[24] The samples in order of smallest spectral contrast and therefore those predicted to be the most vesicular (i.e., have the most blackbody component) were -001, -004 and -005, respectively. The deconvolution-derived vesicularity estimates for these samples were 77%, 73% and 54% (Table 3). Although sample -004 and -005 were from the same block, their spectra had significantly different spectral contrast. In fact, a similar spectral contrast, and hence a similar laboratory-derived vesicularity estimate, was observed for both the ash (-001) and exterior block sample (-004).

[25] The error of this approach for deconvolving laboratory emission spectra is approximately 5% [*Ramsey and Christensen*, 1998; *Ramsey and Fink*, 1999]. However, in order to assess the accuracy of fit of the two end-members, two related statistical errors can be examined. The first is the wavelength-dependant residual error (the measured spectrum minus the modeled spectrum), which shows regions of the spectrum that are not well-modeled by the end-members (Figures 4 and 5). Secondly, the root mean squared (RMS) error is a single value for each model result and is in effect an average of the residual error over the entire wavelength. The RMS error is an accepted value for any least-squares modeling approach and has been

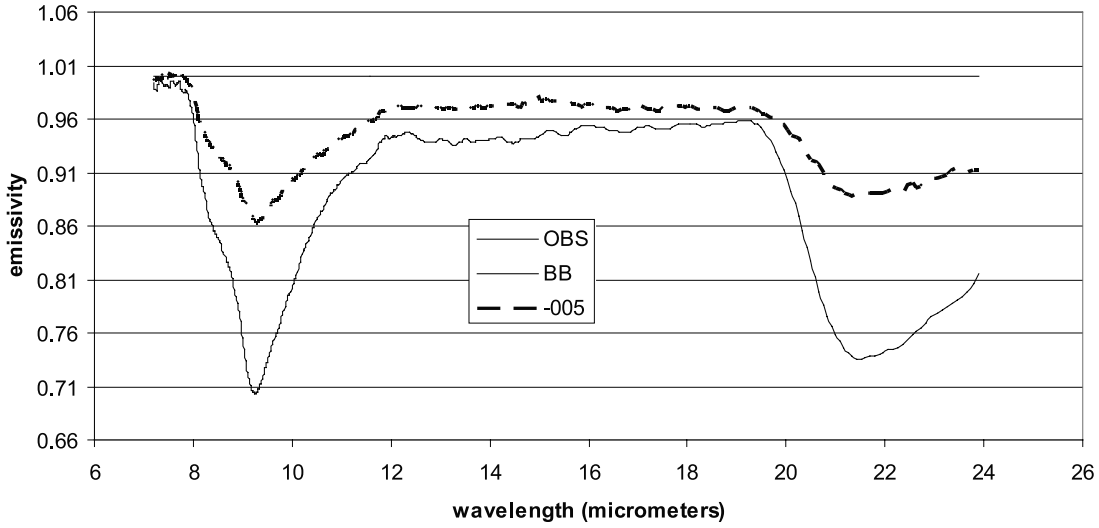

Figure 3. Laboratory thermal infrared (TIR) emission spectra of the two end-members used in this study: obsidian (OBS) and blackbody (BB). Sample -005 is displayed as an example.

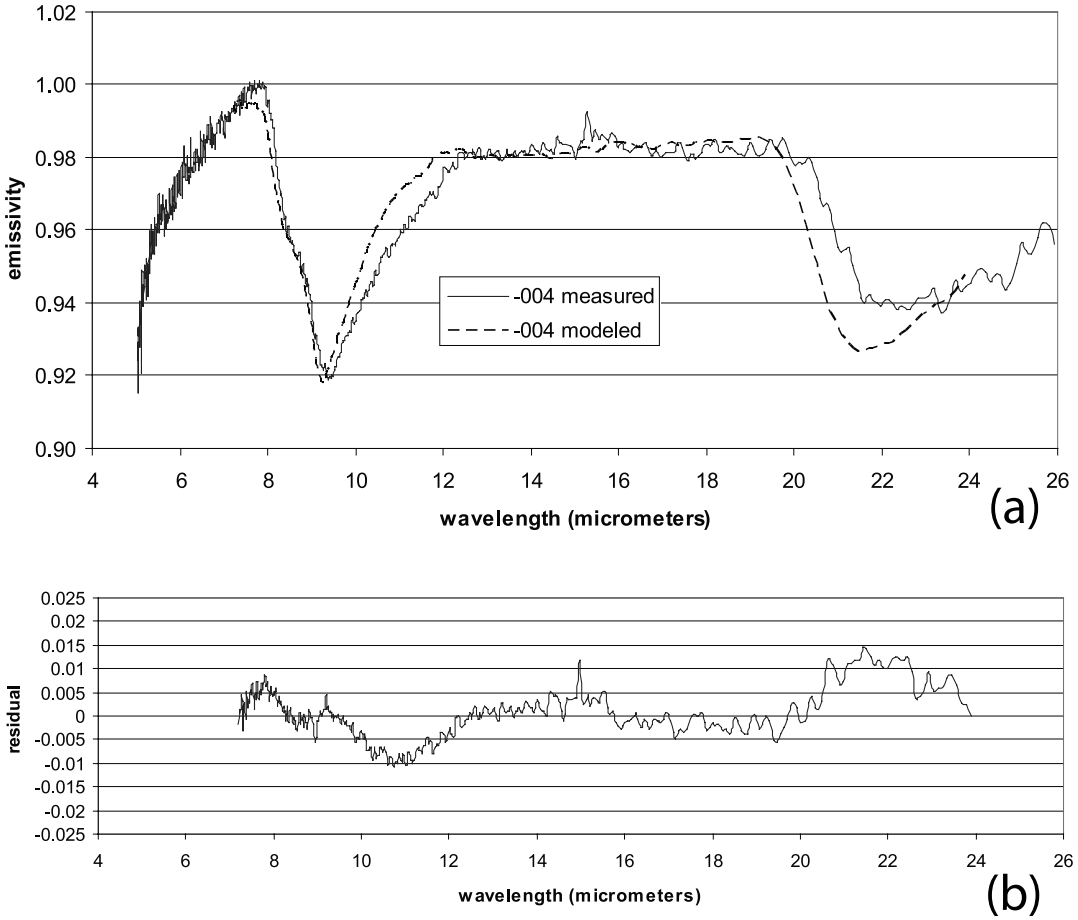

Figure 4. Spectral deconvolution model results for sample -004 performed over the 7–24-μm region. (a) Laboratory emissivity spectra showing the measured spectrum (solid line) and modeled spectrum (dashed line). From 5–7 μm, a decrease in the measured spectrum indicates the presence of fine-grained (<50 μm) particles, likely adhered on the block surface. (b) The residual (measured-modeled) error with most of the discrepancies due to noise in the spectrometer and incomplete removal of atmospheric water vapor and carbon dioxide.

commonly used for the last two decades when reporting the results of spectral deconvolution models. However, it is true that there can be situations where the RMS error is affected by large changes in spectral contrast. One could be misled, for example, when comparing a laboratory-derived RMS error to that of a satellite-based RMS. However, for the case where all samples have similar spectral contrast, as well as for a binary end-member system (both of which are the case here), the RMS and the residual errors are well correlated. In other words, either of these errors are valid in assessing the goodness of fit of a particular model result. For the samples analyzed here the RMS errors were all less than 1%, suggesting a generally good model fit. For completeness, we also show the best (Figure 4) and worst (Figure 5) case residual error results, which range from 0 to 2.5% across the wavelength range studied.

4.3. Satellite-Based TIR Spectra of the Surfaces Sampled

[26] Although the remote sensing data are not a major focus of the work presented here, the ultimate goal is to be able to place accuracy assessments on the use of ASTER data (or other future TIR instruments) to map recently emplaced PF deposits at volcanoes around the world. Five-point ASTER emissivity spectra were extracted for two pixels: area 1 from which samples -004 and -005 were taken (dominantly block-covered) and area 2 from which sample -001 was taken (dominantly ash-covered). A spectral emissivity contrast of 0.02 was noted between the two locations, with a greater contrast in area 1 (Figure 6).

[27] The radiant energy from the surface was from a mixture of blocks and ash on the surface. In order to compensate for these effects and try to correlate laboratory spectral results with those derived from ASTER, we modified the laboratory spectra of the samples on the basis of the estimates of ground cover. For area 1 and 2 (Table 4) a mixed end-member laboratory spectrum was created using the surveyed percentage of blocks and ash. For area 1, a mixed spectrum of 70% of the -004 block spectrum plus 30% the -001 ash spectrum was created. Similarly, for area 2, a mixed spectrum of 10% blocks plus 90% ash was created, again using samples -004 and -001, respectively. Using these end-members as a laboratory-based comparison to the ground cover for areas 1 and 2 the spectral deconvolution model produced vesicularity estimates of 74% and 77%,

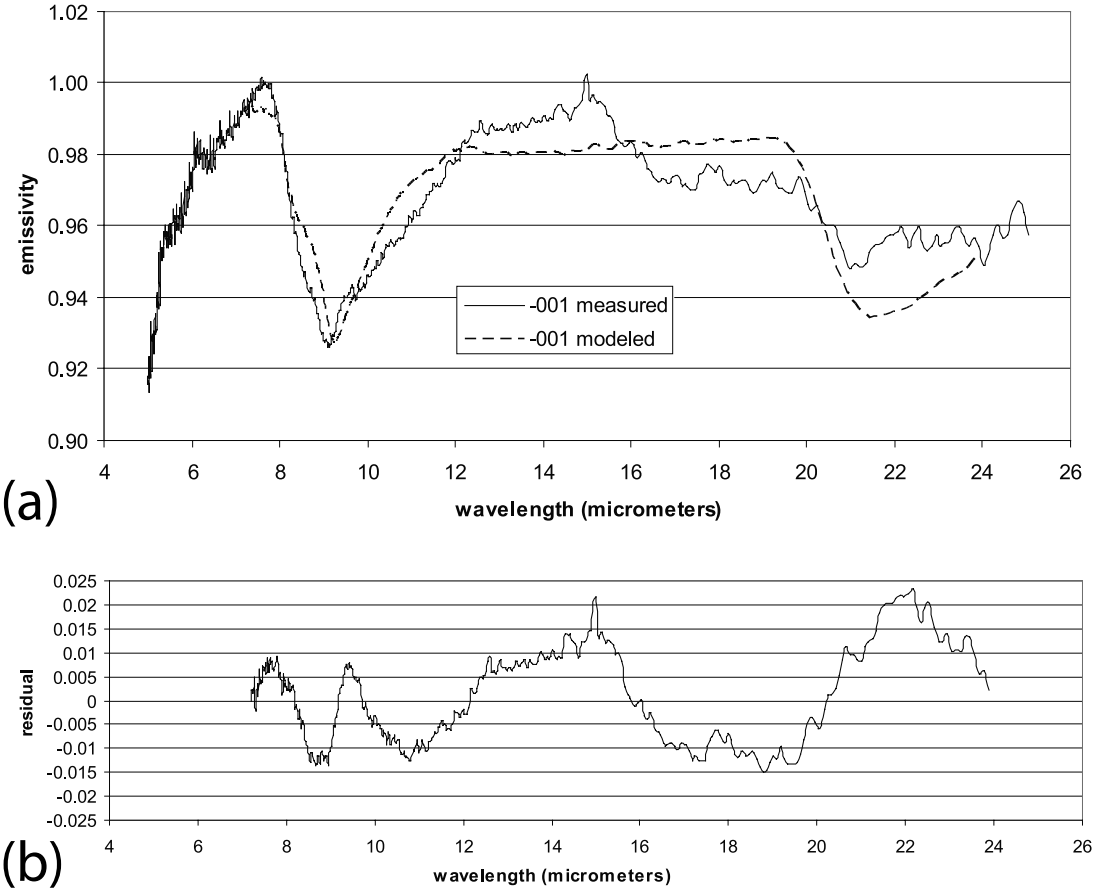

Figure 5. Spectral deconvolution model results for sample -001 performed over the 7–24-μm region. (a) Laboratory emissivity spectra showing the measured spectrum (solid line) and modeled spectrum (dashed line). From 5–7 μm, a similar decrease in the measured spectrum indicates the presence of fine-grained (<50 μm) particles. (b) The residual (measured-modeled) error. Compared to sample -004, there are larger discrepancies throughout the residual spectrum although the overall average difference is still very small.

respectively. This showed a positive correlation with the results derived solely from the ASTER data (Figure 7).

4.4. Comparison of ASTER Satellite-Derived and Laboratory Emissivity Spectra

[28] Satellite-based (ASTER) TIR data at 90 m/pixel spatial resolution were collected on 20 August 2005 (coincident with the field data collection). The data were atmospherically corrected and separated into brightness temperature and surface emissivity. The emissivity spectra for the two field locations were extracted (Figure 6) and visually compared to laboratory-derived spectra over the 8–12-μm region. To test the effects ASTER's lower spectral resolution on the deconvolution model, the laboratory spectra of the field samples and end-members were degraded to ASTER and the deconvolution model reapplied. The average difference between the laboratory and the ASTER resolution was 2% with the maximum being 5% (Table 5). Furthermore, there was no difference between the laboratory-derived and spectrally degraded data for sample -005 (54%). Therefore for the binary deconvolution approach of glass plus blackbody, an error of ±2.5% is assumed as the limit for ASTER-derived modeled vesicularity. This value is nearly identical to the results of *Ramsey and Christensen* [1998] who studied binary compositional mixtures in the laboratory. The laboratory-derived and ASTER-derived vesicularity estimates showed a positive correlation (Figure 7).

4.5. SEM Image-Derived Vesicularity and R_a Results

[29] After averaging the surface roughness profiles of 200 horizontal and 200 vertical profiles, a single R_a value was derived for each sample (Figure 8 and Table 2). The

Table 3. Laboratory Spectral Deconvolution Results

Sample	Block/Particulate	Laboratory-Derived Vesicularity	Total % Summation	Root Mean Squared (RMS) Error
MTU-2006-001-P1	Particulate	77	99.38	0.0087
MTU-2006-001-P4	Particulate	77	99.38	0.0087
MTU-20006-004	Block	73	99.6	0.0049
MTU-2006-005	Block	54	99.61	0.0059

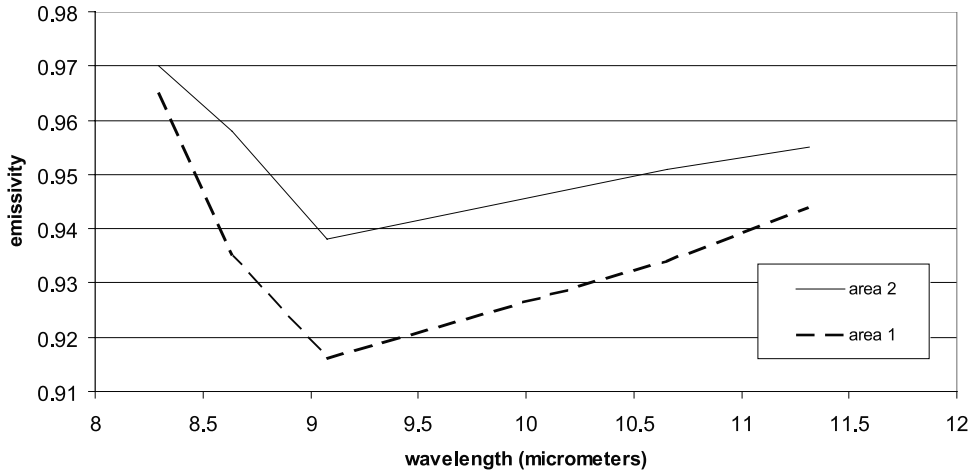

Figure 6. ASTER (acquired on 20 August 2005) TIR emissivity spectra of the 90-m pixel sites in this study. The solid line (area 2, ash-rich site) contained sample MTU 2006-001. The dashed line (area 1, block-rich site) contained sample MTU 2006-004 and -005. The slight reduction in spectral contrast is expected for fine-grained particulate surfaces compared to more block-rich surfaces.

measured range of R_a values was from 0.9 to 2.8 μm. The highest surface roughness value (2.8 μm) was associated with sample -004 and agreed with visual estimates. The least rough surface (0.9 μm) was from sample -001-P4, which contained a small (300 μm long) ash particle. The particulate ash and lapilli samples revealed textural heterogeneities in the 14 March 2000 deposit ranging from 0.9 to 1.3 μm, whereas the coherent block samples from the 11 January

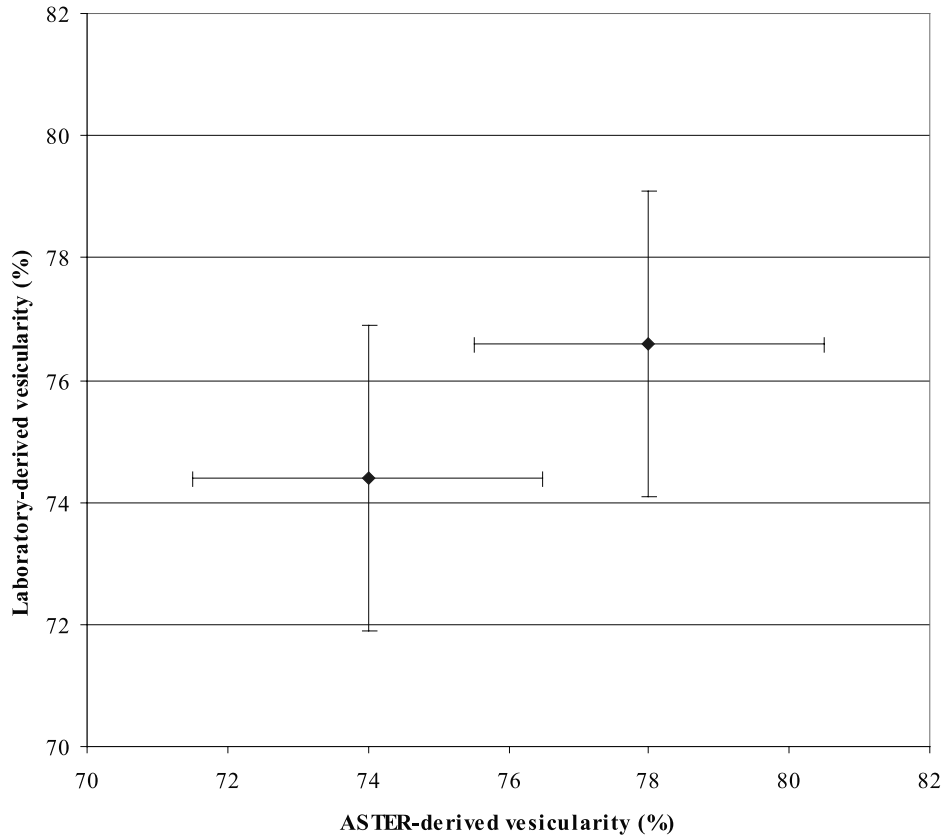

Figure 7. Comparison of ASTER-derived vesicularity results to laboratory-derived vesicularity estimates for area 1 (lower left point) and area 2 (upper right point). An error bar of ±2.5% was placed on the ASTER-derived modeled vesicularity results (see text). Based on the work of *Ramsey and Christensen* [1998], error bars of ±5% were placed on the results derived from the laboratory thermal emission spectra. A positive correlation was observed between both data sets.

Table 4. Comparison of ASTER Deconvolution-Derived Vesicularity Estimates (Taken From 20 August 2005) and Laboratory-Derived Estimates Over Area 1 and Area 2

Area	1	2
Eruption date	Jan 05	Mar 00
Location (UTM, WGS-84)	6200261.35 m N, 601986.869 m E	6199981.77 m N, 602378.80 m E
Laboratory-derived vesicularity	74	77
ASTER-derived vesicularity	49	62
Surface % blocks	70	10
Surface % ash	30	90

2005 eruption produced R_a values of 1.6 to 2.8 μm for the block interior and surface, respectively.

[30] The range of R_a values correlated well with SEM image-derived vesicularity values, which were calculated by using an average of the SEM binary image pairs. The surface vesicularity percentage was calculated and ranged from 18% to 26% (Figure 9). The particulate ash and lapilli samples from the 14 March 2000 deposit had a vesicularity range of 18 to 20%. Comparison of the image-derived vesicularity results to those of the R_a results produced correlation value (R^2) of 0.979 for all samples. If sample -005 (the block interior, which was not a dominant surface component) were removed from the analysis, the correlation value increases to 0.998. Using the terminology of *Houghton and Wilson* [1989], the image-derived vesicularity estimates would classify samples -001-P1 and -001-P4 as incipiently vesicular (5–20%), whereas samples -004 and -005 would classify as poorly vesicular (20–40%). Work from *Belousov et al.* [2002] on the May 1997 PF deposit at Bezymianny showed the average vesicularity was 30%, consistent with the results found in this study.

5. Discussion

[31] Thin section analyses were used to assess the general mineralogy and the vesicularity of the samples at a lower magnification. All samples were characterized by glass and micron-scale roughness elements. The phenocryst areal percentages were generally below the detection limit of the laboratory emission spectroscopy as mineralogic spectral features were not observed. Therefore although the petrologic information did not have a direct bearing on the TIR or SEM results, it does provide insight into the Bezymianny magma system and the processes ongoing during eruption of the pyroclastic material. The higher magnification SEM data provided a positive correlation between the image-derived vesicularity and R_a roughness values, which must be further tested with larger data sets in the future. Although assumed to be true in past studies [e.g., *Ramsey and Fink*, 1999], our results confirm the hypothesis that micron-scale roughness increases as vesicularity increases. These two parameters are linked together as causes of TIR spectral contrast reduction.

[32] The spectroscopy results from areas 1 and 2 derived from both ASTER and the laboratory show a positive correlation. In both spectroscopy data sets the more ash-rich area was modeled as being more vesicular. Of importance is that both techniques show the same general trend and that the values are close to the associated uncertainty for each method. The difference in absolute numbers is not surprising considering that the laboratory data were of small areal spot sizes, acquired at high spectral resolution, and collected in an atmospherically controlled environment. The five-point ASTER data acquired over a 90 m pixel with a model atmospheric correction will always have lower spectral contrast and hence less variation between pixels with variations in ground cover.

Table 5. Comparison of Laboratory-Derived Spectral Deconvolution Results to the Same Spectra that were Resampled to ASTER 5 Point Data and Then Run through the Model

Sample	Laboratory-Derived Vesicularity	Laboratory Spectra Degraded to ASTER 5-Point Result
MTU-2006-001-P4	77	72
MTU-2006-001-P1	77	72
MTU-2006-004	73	72
MTU-2006-005	54	54

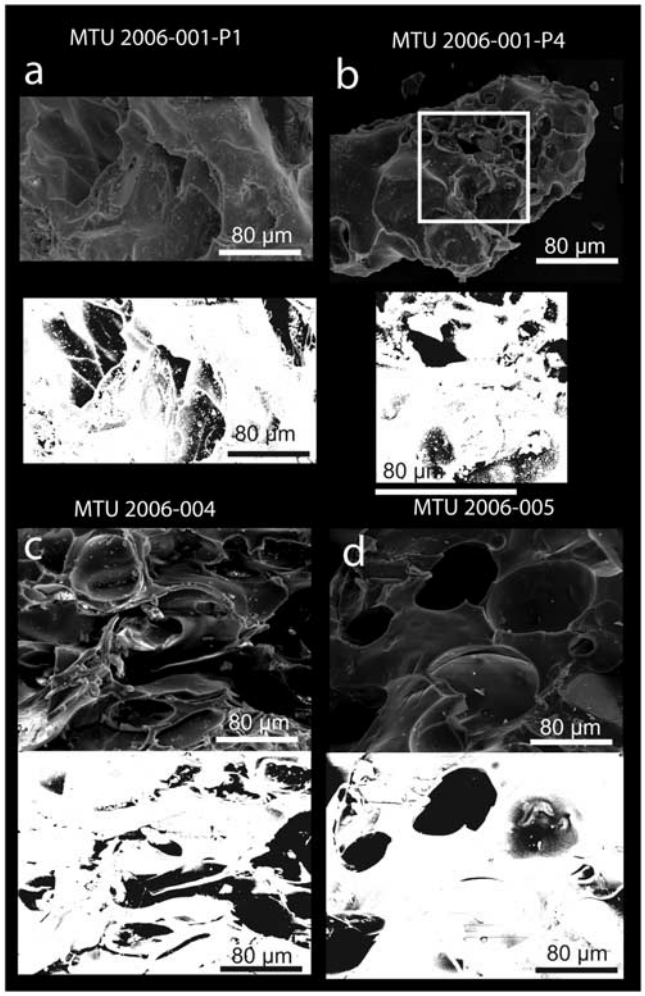

Figure 8. SEM images of the Bezymianny samples and the corresponding binary image below each sample. All images were acquired at a magnification of 400. Samples: (a) -001-P1; (b) 001-P4; (c) -004; (d) -005.

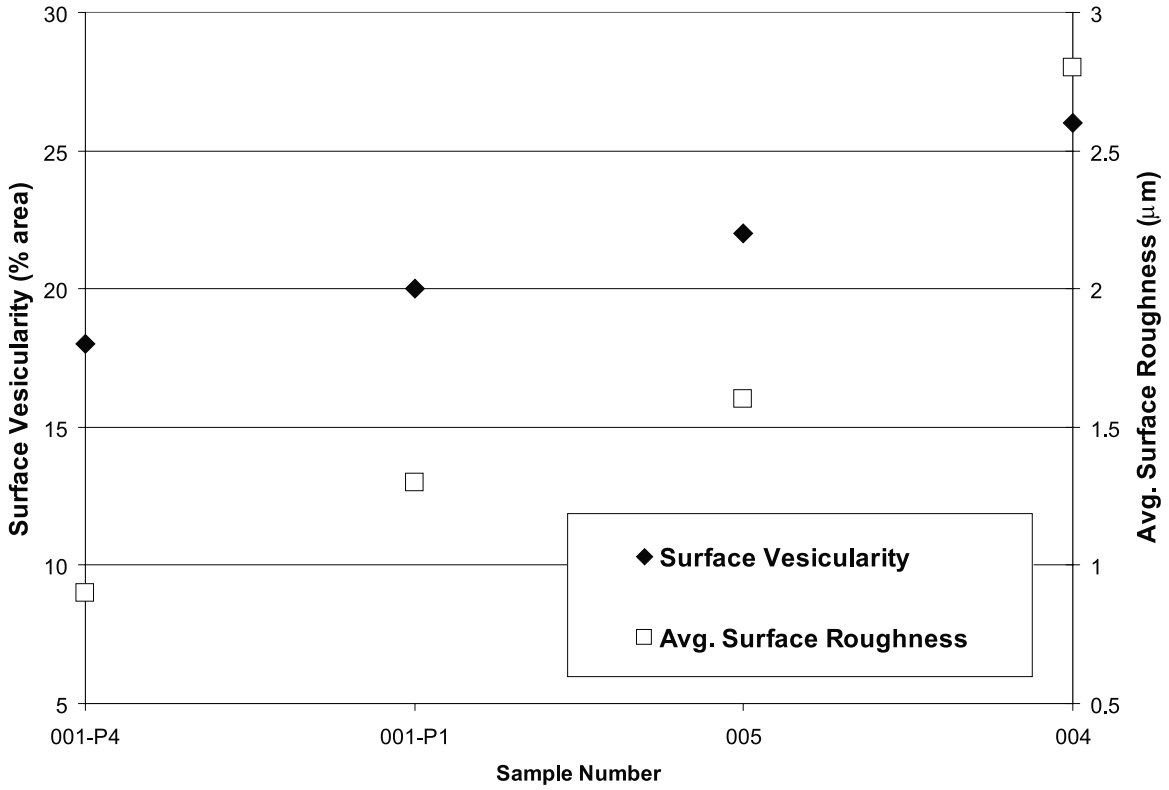

Figure 9. Image-derived surface vesicularity values (see Figure 8 for SEM and binary images) compared to average surface roughness (R_a) values for each sample derived from averaging 400 roughness profiles. A positive correlation between the (R_a) values and image-derived surface vesicularity can be seen.

[33] Using the percentage blackbody as a proxy for the surface vesicularity, the image-derived vesicularity results from the SEM analysis for samples -004 and 005 (26% and 22%, respectively) were substantially lower than the TIR-derived spectroscopy estimates (e.g., 73% and 54%, respectively for the laboratory data). We interpret this discrepancy as being caused by several factors. First and most significantly, the spectroscopy-derived results were overestimated because of the high spectral contrast of the obsidian end-member, relative to the spectra of the samples collected. This end-member has a deep emissivity minimum of 0.68 at ~9 μm (Figure 3) compared to any spectrum from the Bezymianny samples. In a binary deconvolution model, this has the effect of overestimating the blackbody results and hence the TIR-derived vesicularity values. Secondly, using pure rock or mineral spectra as end-members can be problematic for modeling particulate or fine-grained samples, such as the ash-dominated PF surfaces. In studies where spectral contrast is not as critical (e.g., compositional as opposed to textural mapping), a blackbody end-member is commonly added to account for spectral contrast differences between the library end-members and the mixed spectrum. The resulting blackbody end-member percentage can be used as a proxy for the amount of spectral contrast reduction in the mixed spectrum, perhaps indicating the level of atmospheric contamination, the particle sizes on the surface, or the degree to which "self shadowing and re-emission" is present from rough surfaces. However, in most cases this blackbody end-member is removed and the results of the other end-members corrected by normalizing their values so the new totals will sum to 100%. This has worked well for TIR compositional mapping on Mars using a deconvolution approach and a spectral library of mineral end-members with deep spectral contrasts [*Bandfield*, 2002; *Hamilton et al.*, 2003]. This approach is clearly impossible for a study where the blackbody end-member is the critical value, serving as a proxy for surface roughness. For previous studies of lavas, the glass end-member was compared to similar dome rocks and therefore the spectral contrast differences between library and mixed data were negligible. Because the spectral depth of the glass end-member is critical to results of such a modeling approach, ash-rich particulate surfaces are always going to be overestimated in their TIR-derived vesicularity. Thus future work would benefit from the selection of a glassy end-member for PF deposits that can be used to produce more realistic vesicularity estimates. To first order, the current glass end-member could be reduced in spectral contrast artificially to more closely match the results of the SEM data. However, this ad-hoc approach was not presented here as we prefer to display the raw data produced. Further validation of the correct end-member will be carried out on other PF surfaces with a much larger array of field samples in future work.

[34] The laboratory TIR spectral data (see section 4.2) showed a similar spectral morphology and contrast for both the ash sample (-004) and the PF block exterior (-004). This was not expected as the block interior (-005) had a glass-dominated spectral signature (i.e., a greater spectral contrast

and therefore a lower vesicularity). We interpret the spectral similarity of the ash and the exterior of the block as being due to fine particulates adhering to the block surface and in-filling some of the voids. These small fragments were also seen in the SEM images of sample (-004). These fines were likely produced during transport down slope, subsequent eolian transport of the ash onto the block, and/or minor contamination during transport of the block from the field to the laboratory. This contamination by fines has the effect of lowering the spectral contrast and thus increasing the estimated vesicularity results. Therefore although the sample -005 was not a dominant surface type, it may provide a more realistic end-member for future investigations of block-rich PF deposits.

[35] These data, in combination with field investigations from August 2004 and August 2005, provide information on the possible eruption style of the March 2000 and January 2005 eruptions. The March 2000 PF deposit was ash-dominated and deposited over a greater area and longer distance than the January 2005 deposit [*Ramsey and Dehn*, 2004]. The March 2000 eruption column was reported to be relatively low (~8 km) and based on analysis of the deposit we interpret the column as having been relatively gas-depleted, and the PF deposits having been formed by a boil-over style column collapse. In contrast, the January 2005 deposit was composed almost entirely of blocks (e.g., Figure 1). The travel distance was shorter and the areal extent smaller than the March 2000 deposit. On the basis of this and in combination with additional TIR data [*Carter et al.*, 2007], we interpret that the eruption style was different than the 2000 event, with the PF deposit being created primarily from a partial dome collapse, producing a block and ash flow.

6. Conclusions

[36] A clear positive correlation was demonstrated between image-derived vesicularity and R_a values in the PF deposit samples from Bezymianny. Using the image-derived vesicularity estimates as the predicted ground truth, we interpret that the block samples (-004 and -005) were the most vesicular, relative to the ash sample (-001). Therefore a PF deposit covered entirely with blocks would produce a more realistic set of laboratory- and satellite-derived vesicularity results whereas an ash-dominated deposit must be more carefully analyzed. Micron-scale roughness that is not attributed to vesicularity, combined with particle size effects (clearly seen in emissivity spectra shortward of 8 μm in Figures 4 and 5) are the primary causes of modeling error for ash-rich surfaces. Care must therefore be taken when interpreting spectral contrast reduction using satellite- and laboratory-derived data.

[37] We have determined the first spectral deconvolution-derived vesicularity estimates of PF deposit samples. We interpret that column-collapse produced the ash-rich PF deposit in March 2000 and that dome collapse generated a block and ash flow deposit in January 2005. A greater number of samples will aid in validating these initial results. However, we clearly demonstrated the utility of comparing multiple data sets and their interrelationships from the micron- to the tens of meters scale and the value of using TIR spectroscopy data. This work can now be further tested and refined using samples from the 2005–2007 PF deposits at Bezymianny volcano [*Carter et al.*, 2007, 2008] and at other volcanic systems around the world. When analyzing TIR remote sensing data sets for other PF deposits, careful interpretation should provide a framework for future investigations at other rapidly changing, active volcanic surfaces.

[38] **Acknowledgments.** The authors sincerely thank Victoria Hamilton and Shawn Wright for their detailed and helpful reviews that significantly improved the manuscript. This work was funded partially by grants to M.S.R. from the National Aeronautics and Space Administration (NASA) (grant NNG04GO69G), the ASTER Science Team, and the National Science Foundation (NSF) (grant EAR-0309631). For A.J.C., funding was provided by the Andrew Mellon Fellowship and the Henry Leighton Memorial Scholarship. The authors thank Andreas Auer and Susan Wacaster for sample collection and field assistance, Marina Belousova for field assistance and GPS data collection, Nerissa Lindenfelser for edits, Margaret Johnson for assistance in SEM data collection, and Sonja Melander for data processing assistance. The authors also gratefully acknowledge Owen Mills for his kind assistance with the SEM data collection and general advice. A.J.D. gratefully acknowledges support from the MTU GMES fund.

References

Abrams, M. (2000), The Advanced Spaceborne Thermal Emission and Reflectance Radiometer (ASTER): Data products for the high spatial resolution imager on NASA's Terra platform, *Int. J. Remote Sens.*, *21*, 847–859.

Adams, J. B., M. O. Smith, and P. E. Johnson (1986), Spectral mixture modeling: A new analysis of rock and soil types at the Viking Lander I site, *J. Geophys. Res.*, *91*, 8098–8112.

Anderson, S. W., and J. H. Fink (1990), The development and distribution of lava textures at the Mount St. Helens dome, in *Lava Flows and Domes: Emplacement Mechanisms and Hazard Implications*, edited by J. H. Fink, *IAVCEI Proc. Volcanol.*, *2*, 25–46.

Bandfield, J. (2002), Global mineral distributions on Mars, *J. Geophys. Res.*, *107*(E6), 5042, doi:10.1029/2001JE001510.

Belousov, A., B. Voight, M. Belousova, and A. Petukhin (2002), Pyroclastic surges and flows from the 8–10 May 1997 explosive eruption of Bezymianny volcano, Kamchatka, Russia, *Bull. Volcanol.*, *64*, 455–471.

Bogoyavlenskaya, G. E., and I. T. Kirsanov (1981), Twenty five years of volcanic activity of Bezymianny (in Russian), *Volcanol. Seismol.*, *2*, 3–13.

Bogoyavlenskaya, G. Y., O. A. Braitseva, I. V. Melekestev, A. P. Maksimov, and B. V. Ivanov (1991), Bezymianny Volcano, in *Active Volcanoes of Kamchatka*, vol. 1, edited by S. A. Fedotov and Y. P. Masurenkov, pp. 168–197, Nauka, Moscow, Russia.

Byrnes, J. M., M. S. Ramsey, and D. A. Crown (2004), Surface unit characterization of the Mauna Ulu flow field, Kilauea Volcano, Hawai'I, using integrated field and remote sensing analyses, *J. Volcanol. Geotherm. Res.*, *135*, 169–193.

Byrnes, J. M., M. S. Ramsey, P. L. King, and R. J. Lee (2007), Thermal infrared reflectance and emission spectroscopy of quartzofeldspathic glasses, *Geophys. Res. Lett.*, *34*, L01306, doi:10.1029/2006GL027893.

Carter, A. J., M. S. Ramsey, A. J. Durant, and I. P. Skilling (2006), Multi-temporal three dimensional imaging of volcanic products on the macro- and micro-scale, *Eos Trans. AGU*, *87*(52), Fall Meet. Suppl., Abstract V53B-1752.

Carter, A. J., M. S. Ramsey, and A. B. Belousov (2007), Detection of a new summit crater on Bezymianny Volcano lava dome: Satellite and field-based thermal data, *Bull. Volcanol.*, *69*, 811–815.

Carter, A. J., O. A. Girina, M. S. Ramsey, and Yu. Demyanchuk (2008), ASTER and field observations of the 24 December 2006 eruption of Bezymianny Volcano, Russia, *Remote Sens. Environ.*, *112*, 2569–2577.

Christensen, P. R., J. L. Bandfield, V. E. Hamilton, D. A. Howard, M. D. Lane, J. L. Piatek, S. W. Ruff, and W. L. Stefanov (2000), A thermal emission spectral library of rock-formation minerals, *J. Geophys. Res.*, *105*, 9735–9739.

Crisp, J., A. B. Kahle, and E. A. Abbott (1990), Thermal infrared spectral character of Hawaiian basaltic glasses, *J. Geophys. Res.*, *95*, 21,657–21,669.

Feely, K. C., and P. R. Christensen (1999), Quantitative compositional analysis using thermal emission spectroscopy: Application to igneous and metamorphic rocks, *J. Geophys. Res.*, *104*, 24,195–24,210.

Francis, P. W., G. Wadge, and P. J. Mouginis-Mark (1996), Satellite monitoring of volcanoes, in *Monitoring and Mitigation of Volcano Hazards*, edited by R. Scarpa and R. Tilling, pp. 257–298, Springer, New York.

Goldstein, J. I., D. E. Newbury, P. Echlin, D. C. Joy, C. Fiori, and E. Lifshin (1981), *Scanning Electron Microscopy and X-Ray Microanalysis*, 673 pp., Springer, New York.

Gorshkov, G. S. (1959), Gigantic eruption of the Bezymianny volcano, *Bull. Volcanol.*, *20*, 77–109.

Hamilton, V. E., and P. R. Christensen (2000), Determining of modal mineralogy of mafic and ultramafic igneous rocks using thermal emission spectroscopy, *J. Geophys. Res.*, *105*, 9717–9734.

Hamilton, V. E., P. R. Christensen, H. Y. McSween Jr., and J. L. Bandfield (2003), Searching for the source regions of Martian meteorites using MGS TES: Integrating Martian meteorites into the global distribution of volcanic materials on Mars, *Meteorit. Planet. Sci.*, *38*, 871–885.

Heiken, G., and K. H. Wohletz (1985), *Volcanic Ash*, 246 pp., Univ. of Calif. Press, Berkeley.

Houghton, B. F., and C. J. N. Wilson (1989), A vesicularity index for pyroclastic deposits, *Bull. Volcanol.*, *51*, 451–462.

International Standard Norme Internationale (1997), *Geometrical Product Specifications (GPS)—Surface Texture: Profile Method—Terms, Definitions and Surface Texture Parameters*, Global Engineering Documents, ISO document 4287, 1st ed., 18 pp.

Kamchatka Volcanic Eruption Response Team (KVERT) Report (2005), Bezymianny Volcano, 11 January 2005. (Available at http://www.avo.alaska.edu/activity/avoreport.php?view=kaminfo&id=47&type=kaminfo&month=January&year=2005)

Kamchatka Volcanic Eruption Response Team (KVERT) Online Archive (2007), Volcanoes of Kamchatka: Bezymianny. (Available at http://www.kscnet.ru/ivs/kvert/volcanoes/Bezymianny/index_eng.html)

King, P. L., M. S. Ramsey, P. F. McMillan, and G. Swayze (2004), Laboratory Fourier transform infrared spectroscopy methods for geologic samples, in *Infrared Spectroscopy in Geochemistry, Exploration, and Remote Sensing*, vol. 33, edited by P. King, M. Ramsey, and G. Swayze, pp. 57–91, Mineral. Assoc. of Canada, London, Ont.

Kirkland, L. E., K. C. Herr, E. R. Keim, P. M. Adams, J. W. Salisbury, J. A. Hackwell, and A. Treiman (2002), First use of a thermal infrared hyperspectral scanner for compositional mapping, *Remote Sens. Environ.*, *80*, 447–459.

Klug, C., and K. V. Cashman (1994), Vesiculation of the May 18, 1980, Mount St. Helens magma, *Geology*, *22*, 468–472.

Lyon, R. J. P. (1965), Analysis of rocks by spectral infrared emission (8 to 25 microns), *Econ. Geol.*, *60*, 715–736.

Minnich, B., H. Bartell, H. Leeb, E. W. N. Bernroider, W. D. Krautgartner, and A. Lametschwandtner (2001), Quantification of microvasculature by SEM and 3D morphometry, *Microsc. Anal.*, *15*, 27–29.

Minitti, M. E., V. E. Hamilton, and M. B. Wyatt (2007), Deconvolution of Martian thermal infrared spectra using a simplified, glass-rich library, paper presented at 38th Lunar Plan. Sci. Meet., Houston.

Moersch, J. E., and P. R. Christensen (1995), Thermal emission from particulate surfaces: A comparison of scattering models with measured spectra, *J. Geophys. Res.*, *100*, 7465–7477.

Moersch, J. E., K. A. Horton, P. G. Lucey, and S. W. Ruff (2002), Characterization of target adjacency effects in horizontal-viewing thermal infrared spectroscopy, with applications to the MER Mini-TES experiment, *33rd Proc. Lunar Planet. Sci. Conf.* (Available at http://www.mars.asu.edu/christensen/docs/moersch_hapke_jgr.pdf)

Nakada, S., Y. Miyake, H. Sato, O. Oshima, and A. Fujinawa (1995), Endogenous growth of dacite dome at Unzen volcano (Japan), 1993–1994, *Geology*, *23*, 157–160.

Ondrusek, J., P. R. Christensen, and J. H. Fink (1993), Mapping the distribution of vesicular textures on silicic lavas using the Thermal Infrared Multispectral Scanner, *J. Geophys. Res.*, *98*, 15,903–15,908.

Podsiadlo, P., and G. W. Stachowiak (1997), Characterization of surface topography of wear particles by SEM stereoscopy, *Wear*, *206*, 39–52.

Ramsey, M. S., and J. Dehn (2004), Spaceborne observations of the 2000 Bezymianny, Kamchatka eruption: The integration of high-resolution ASTER data into near real-time monitoring using AVHRR, *J. Volcanol. Geotherm. Res.*, *135*, 127–146.

Ramsey, M. S., and J. H. Fink (1999), Estimating silicic lava vesicularity with thermal remote sensing: A new technique for volcanic mapping and monitoring, *Bull. Volcanol.*, *61*, 32–39.

Ramsey, M. S., and P. R. Christensen (1998), Mineral abundance determination: Quantitative deconvolution of thermal emission spectra, *J. Geophys. Res.*, *103*, 577–596.

Rasband, W. S. (1997), ImageJ, U.S. National Institutes of Health, Bethesda, Md. (Available at http://rsb.info.nih.gov/ij/)

Realmuto, V. J. (1990), Separating the effects of temperature and emissivity: Emissivity spectrum normalization, in *Proceedings of the Second Annual Airborne Earth Science Workshop*, vol. 2, edited by E. A. Abbott, pp. 31–35, Jet Propul. Lab., Pasadena, Calif.

Ruff, S. W., P. R. Christensen, P. W. Barbera, and D. L. Anderson (1997), Quantitative thermal emission spectroscopy of minerals: A laboratory technique for measurement and calibration, *J. Geophys. Res.*, *102*, 14,899–14,913.

Sarda, P., and D. Graham (1990), Mid-ocean ridge popping rocks: Implications for degassing at ridge crests, *Earth Planet. Sci. Lett.*, *97*, 268–289.

Song, S.-R., K. W. Jones, B. W. Lindquist, B. A. Dowd, and D. L. Sahagian (2001), Synchrotron X-ray computed microtomography: Studies on vesiculated basaltic rocks, *Bull. Volcanol.*, *63*, 252–263.

Thomas, T. R. (1999), *Rough Surfaces*, 2nd ed., 278 pp., Imperial College Press, London, U.K.

Thomson, J. L., and J. W. Salisbury (1993), The mid-infrared reflectance of mineral mixtures (7–14 microns), *Remote Sens. Environ.*, *45*, 1–13.

Vaughan, R. G., S. J. Hook, M. S. Ramsey, V. J. Realmuto, and D. J. Schneider (2005), Monitoring eruptive activity at Mount Saint Helens with TIR image data, *Geophys. Res. Lett.*, *32*, L19305, doi:10.1029/2005GL024112.

Watts, R. B., R. A. Herd, R. S. J. Sparks, and S. R. Young (2002), Growth patterns and emplacement of the andesitic lava dome at Soufrière Hills Volcano, Montserrat, in *The Eruption of Soufrière Hills Volcano, Montserrat, From 1995 to 1999*, edited by T. Druitt and P. Kokelaar, *Geol. Soc. London Mem.*, *21*, 115–152.

Yamaguchi, Y., A. B. Kahle, H. Tsu, T. Kawakami, and M. Pniel (1998), Overview of Advanced Spaceborne Thermal Emission and Reflection Radiometer (ASTER), *IEEE Trans. Geosci. Remote Sens.*, *36*, 1062–1071.

A. J. Carter, M. S. Ramsey, I. P. Skilling, and A. Wolfe, Department of Geology and Planetary Science, University of Pittsburgh, 200 SRCC Building, 4107 O'Hara Street, Pittsburgh, PA 15260-3332, USA. (ajc44@pitt.edu)

A. J. Durant, Geological Sciences, Michigan Technological University, Dow 630, 1400 Townsend Drive, Houghton, MI 49931, USA.